Archives of Hydro-Engineering and Environmental Mechanics
Vol. 57 (2010), No. 1, pp. 3–30

Effect of Grain Crushing on Shear Localization in Granular Bodies within Micro-Polar Hypoplasticity

Jacek Tejchman

Faculty of Civil and Environmental Engineering Gdańsk University of Technology,
80-233 Gdańsk, ul. Narutowicza 11/12, Poland, e-mail: tejchmk@pg.gda.pl

(Received June 22, 2009; revised January 28, 2010)

Abstract

The paper deals with the effect of grain crushing on shear localization in granular materials in an infinite long narrow granular strip under constant vertical pressure. The calculations were carried out with an enhanced micro-polar hypoplastic constitutive model which is able to describe the salient properties of crushable granular bodies including shear localization. The change of the mean grain diameter with varying pressure was taken into account with the help of formulae from breakage mechanics. The effect of pressure and initial void ratio on shear localization was studied.

Key words: breakage mechanics, grain crushing, micro-polar hypoplasticity, sand, shearing

1. Introduction

Grain crushing is one of the phenomena which may strongly influence the stress-strain behaviour of granular bodies. It occurs under compression or shear when the energy available is sufficient to overcome the resistance of the material (indentation strength, abrasive hardness or tensile strength) (Miura and O'Hara 1979, Hardin 1985, Turcotte 1986). Since it is an inherent characteristics of these deformation processes, it should be taken into account in constitutive modelling. It is particularly important when describing shear localization since the thickness of shear zones depends, among others, on the mean grain diameter, which diminishes during particle crushing.

The phenomenon of particle degradation was experimentally investigated by Nakata et al (2001) during one-dimensional compression, Indraratna and Salim (2002) during triaxial compression, Coop et al (2004) in a ring shear apparatus and Arslan et al (2009) in a direct shear test.

The experimental results show that particle breakage influences the stress-strain behaviour. It increases with increasing grain brittleness and confining pressure. It is affected by grain angularity, grain size distribution, grain diameter, particle

strength, porosity, uniformity of gradation, stress level and anisotropy. It also rises with increasing shear strain at a decreasing rate. It is accompanied by volumetric compression and occurs even at low confining stresses, but in lower rates. Due to crushing, the dilatative behaviour of granulates is suppressed. Larger particles are more vulnerable to degradation in terms of their strength but more resistive, for they tend to be more cushioned (McDowell et al 1996). The particle breakage is greater for uniformly graded than for well-graded granulates. A constant grading is reached at very large strains only. The initial grain size distribution *gsd* tends to evolve towards an ultimate fractal distribution (Hardin 1985). Due to particle breakage, the critical state line changes (Yamamuro and Lade 1998). In turn, the mobilized residual strength is not affected by breakage. The particle breakage is usually stronger in the shear zone than outside it.

Grain crushability has been studied theoretically by a number of researchers (e.g. Indraratna and Salim (2002) and by Einav (2007a)) using a continuum approach and by e.g. Cheng et al (2003), Marketos and Bolton (2007) and Vallejo and Lobo-Guerrero (2009) using a discrete element model DEM. Of particular interest to the current paper is the formulation of the breakage mechanics theory (Einav 2007a, 2007b, 2007c, Einav and Valdes 2008), which is capable of explaining the above properties of behaviour through energy considerations.

The intention of the paper is to explore the effect of grain crushing, expressed by a change of the mean grain diameter, on shear localization in granular materials, during quasi-static shearing of an infinite long narrow granular strip under different vertical pressures. The calculations were carried out with a hypoplastic continuum constitutive model enhanced by a varying mean grain diameter. This enhanced model is able to capture the salient properties of granular bodies, including shear localization and crushing. The change of the mean grain diameter with varying pressure ratio was taken into account with the help of formulae from breakage mechanics proposed by Einav (2007a, 2007b) and Einav and Valdes (2008). In addition, the effect of initial void ratio on particle breakage was taken into account. The effect of grain crushing on shear localization has not been numerically investigated yet.

2. Micro-Polar Hypoplastic Constitutive Model without Particle Breakage

Despite the discrete nature of granular materials, the mechanical behaviour of confined configurations in the quasi-static regime can be reasonably described by the principles of continuum mechanics. Non-polar hypoplastic constitutive models have been developed at Karlsruhe University (Gudehus 1996, Bauer 1996), where the stress rate tensor is assured to depend on stress, strain rate and void ratio via isotropic non-linear tensorial functions based on the representation theorem. The constitutive models were formulated by a heuristic process considering the essential mechanical properties of granular materials undergoing homogeneous deformation.

A striking feature of hypoplasticity is that the constitutive equation is incrementally nonlinear in deformation rate. The hypoplastic models are capable of describing some salient properties of granular materials, e.g. non-linear stress-strain relationship, dilatant and contractant volumetric change, stress level dependence, density dependence and strain softening. A further feature of hypoplastic models is the inclusion of the critical states, i.e. states in which a grain aggregate can deform continuously at constant stress and volume (void ratio). Moreover, both the coaxiality (coincidence of the direction of the principal stresses and principal plastic strain increments) and stress-dilatancy rule are not assumed a priori (Tejchman and Wu 2009). In contrast to elasto-plastic models, a decomposition of deformation into elastic and plastic parts, the formulation of a yield surface, plastic potential, flow rule and hardening rule are not needed. In spite of the fact that the failure surface and flow rule are not prescribed in hypoplasticity, they emerge as by-products (Wu and Niemunis 1996). The hallmarks of these models are their simple formulation and procedure for determining material parameters with standard laboratory experiments. The material parameters can be related to the granulometric properties of granular materials, such as grain size distribution curve, shape, angularity and hardness of grains (Herle and Gudehus 1999). A further advantage lies in the fact that one single set of material parameters is valid for a wide range of pressures and densities.

Hypoplastic constitutive models without a characteristic length cannot describe the scale effects associated with shear zones, such as thickness and spacing of shear zones. A characteristic length can be introduced into hypoplasticity by means of either the micro-polar, or non-local or second-gradient theory (Tejchman 2004). In this paper, a micro-polar theory is adopted. A micro-polar model makes use of rotations and couple stresses, which have clear physical meaning for granular materials. First, the rotations and couple stresses can be observed during shearing and remain negligible during homogeneous deformation (Oda 1993). Second, Pasternak and Mühlhaus (2001) have demonstrated that the additional rotational degree of freedom of a micro-polar continuum arises naturally by mathematical homogenization of an originally discrete system of spherical grains with contact forces and contact moments.

A micro-polar continuum considers the deformation at two different levels: micro-rotation at the particle level and macro-deformation at the structural level (Schäfer 1962). For the case of plane strain, each material point has three degrees of freedom: two translations u_i and one independent rotation ω^c (Fig. 1a). The gradients of the rotation are related to the curvatures, which are associated with the couple stresses through constitutive equations (Fig. 1b). The presence of the couple stresses gives rise to a non-symmetric stress tensor and a characteristic length.

The summary of the micro-polar hypoplatic constitutive law (Tejchman and Gudehus 2001, Tejchman 2004, Tejchman and Wu 2007, 2009) for plane strain is given in the Appendix. The changes of the values of e_i, e_d and e_c decrease with

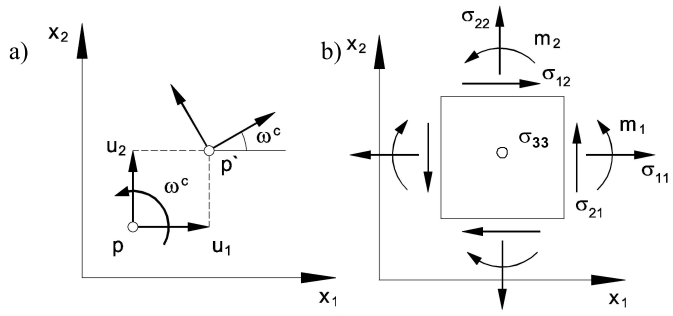

Fig. 1. Plane strain static Cosserat continuum (without body forces and moment): a) degrees of freedom (u_1 – horizontal displacement, u_2 – vertical displacement, ω^c – Cosserat rotation), b) stresses σ_{ij} and couple stresses m_i at an element

the pressure σ_{kk} according to the exponential functions (Eqs. 57–59 in Appendix) (Bauer 1996). In general, the above constitutive model requires the following ten material parameters: e_{i0}, e_{d0}, e_{c0}, ϕ_c, h_s, β, n, α, a_c and d_{50}. The calibration procedure for the non-polar model and the material parameters for different sands were given by Bauer (1996), and Herle and Gudehus (1999). The parameters h_s and n can be estimated from a single oedometric compression test with an initially loose specimen (h_s reflects the slope of the curve in a semi-logarithmic representation, and n its curvature). The parameters α and β can be determined from a triaxial or plane strain test with a dense specimen. The critical friction angle ϕ_c can be determined from the angle of repose or measured in a triaxial test with a loose specimen. The parameters of e_{i0}, e_{d0}, e_{c0} and d_{50} are obtained from conventional index tests ($e_{c0} \approx e_{\max}, e_{d0} \approx e_{\min}, e_{i0} \approx (1.1 - 1.5)e_{\max}$). The FE-analyses were carried out with the following material constants for so-called "Karlsruhe" sand ($d_{50} = 0.5$ mm): $e_{i0} = 1.30$, $e_{d0} = 0.51$, $e_{c0} = 0.82$, $\phi_c = 30°$, $h_s = 190.0$ MPa, $\beta = 1$, $n = 0.50$, $\alpha = 0.30$ and $a_c = a_1^{-1}$. It is important to note that these material parameters were determined in laboratory tests with grain crushing.

3. Grain Crushing

The degree of grain size reduction is quantified by introducing fundamental formulae from breakage mechanics (Einav 2007a, 2007b, Einav and Valdes 2008), i.e. a constitutive theory that couples stresses, strains and the evolving property of the grain size distribution *gsd* (one of the main properties influencing the constitutive behaviour of granular bodies). Breakage mechanics theory can be used as an independent constitutive modelling framework which is consistent with the laws of thermodynamics (Einav 2007a). Contrasted to the hypoplastic modelling framework, the thermodynamics of rate-independent dissipative materials entail definitions of yield functions and flow rules. Within the yield surface, the behaviour is elastic. The yield function and flow rule are activated upon yielding, which is directly

connected to hypothesized energy balanced. The energy balance postulate (Einav 2007b) enables one to describe how the grain size distribution *gsd* evolves via the property of breakage as a thermodynamics internal variable. The evolution law for an average grain size developed within breakage mechanics was simply put into a micro-polar hypoplastic model to learn about grain size reduction in the infinite shear layer subjected to shearing under constant vertical pressure.

It is assumed in breakage mechanics that the current *gsd* can be scaled from the initial and ultimate *gsd* via the breakage internal variable B, which can be measured at any time of testing, effectively by unloading the sample and subsequently sieving the particles. It denotes the ratio of the areas entrapped between the current, initial and ultimate *gsd* on the cumulative semi-logarithmic scale (Fig. 2a).

The energy potential ψ and dissipation potential Φ are assumed to take the following form in breakage mechanics, by assuming linear elasticity within the yield surface (Einav 2007a, 2007b, 2007c):

$$\Psi = \frac{1}{2}(1 - \vartheta B)K\varepsilon_v^{e2} + 3G\varepsilon_s^{e2}, \tag{1}$$

$$\Phi = \sqrt{\Phi_B^2 + \Phi_p^{v2} + \Phi_P^{s2}}, \tag{2}$$

where K denotes the bulk modulus, G is the shear modulus, ε_v^e is the elastic volumetric strain and ε_s^e denotes the elastic shear strain. The parameter ϑ denotes a grading index in terms of the proximity of the initial *gsd* to the ultimate one. The definition of the grading index is the product of statistical homogenization that accounts for the scaling of the specific strain energy at the different particles as a function of their size. It takes the form

$$\vartheta = 1 - \frac{\left\langle d^2 \right\rangle_u}{\left\langle d^2 \right\rangle_0}, \tag{3}$$

where d represents the grain size, and $\left\langle d^2 \right\rangle_u$ and $\left\langle d^2 \right\rangle_0$ denote the second order moments of the ultimate and initial *gsd* functions, respectively.

The breakage scalar variable B weighs a relative distance of the current *gsd* $p(x)$ from the initial and ultimate *gsd's* $p_0(x)$ and $p_u(x)$ (Fig. 2a)

$$p(x) = p_0(x)(1 - B) + p_u(x)B. \tag{4}$$

The term $1 - \vartheta B$ in Eq. 1 is similar to the term (1-D) in damage mechanics (D – damage variable). The parameter $B = 0$ denotes unbroken material and $B = 1$ represents complete breakage. The dissipation potential Φ (being combination of plastic and breakage components) comprises three parts corresponding to breakage dissipation Φ_B, plastic volumetric dissipation Φ_p^v and plastic shear dissipation Φ_p^s (of the Coulomb type), respectively (Einav 2007b):

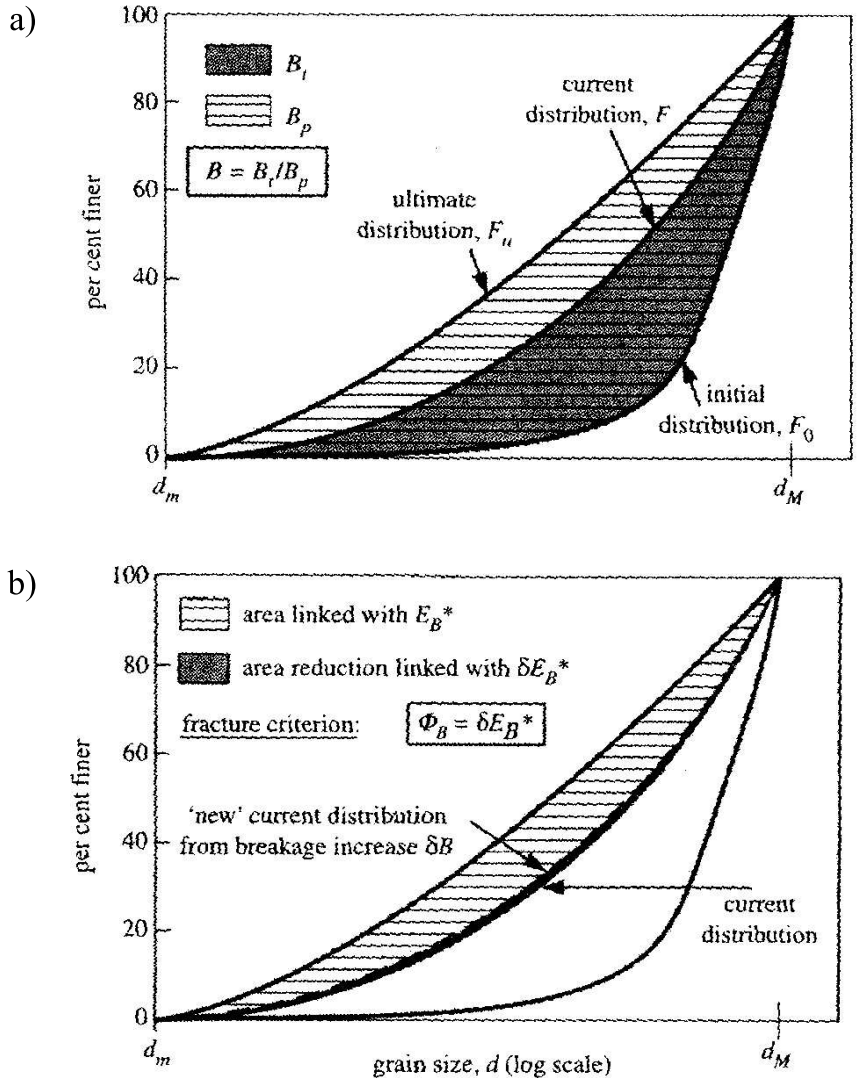

Fig. 2. Breakage mechanics: a) definition of breakage, b) breakage propagation criterion (d_m – minimum grain diameter, d_M – maximum grain diameter) (Einav 2007c)

$$\Phi_B = \frac{E_B}{\cos\omega}\delta B = \frac{\sqrt{E_B E_c}}{(1-B)\cos\omega}\delta B, \tag{5}$$

$$\Phi_p^v = \frac{p}{\sin\omega}\delta\varepsilon_v^p = \frac{p}{(1-B)\sin\omega}\sqrt{\frac{E_c}{E_B}}\delta\varepsilon_v^p, \tag{6}$$

$$\Phi_p^s = q\left|\delta\varepsilon_s^p\right| = Mp\left|\delta\varepsilon_s^p\right| \tag{7}$$

with

$$M = \frac{6\sin\phi}{3-\sin\phi}, \tag{8}$$

$$E_B = \frac{E_c}{(1-B)^2}, \tag{9}$$

where ω – the plastic-breakage coupling angle necessary to link grain crushing and plastic volumetric deformation, M – the ratio between the second deviatoric stress invariant $q\left(q = \sqrt{\frac{3}{2}s_{ij}s_{ij}}\right)$ and mean pressure $pp = \sigma_{ii}/3$ at material failure, ϕ – the internal friction angle at failure calculated with principal stresses, s_{ij} – the stress deviator (δ – increment). The parameter E_B denotes the non-negative breakage energy describing the total stored energy that is released from the system during the fracturing from the beginning state of the initial particle distribution to the final state of the ultimate grain size distribution. The critical energy E_c is related to the crushing pressure in isotropic compression

$$E_c = \frac{p_c^2\vartheta}{2K}. \tag{10}$$

In turn, the parameter E_B^* is the residual breakage energy, i.e. energy reserved in the system for breaking the particles at any given moment, i.e. from the current state to the ultimate state. Between the two energies is the relationship

$$E_B = \frac{E_B^*}{1-B}. \tag{11}$$

The incremental reduction in the residual breakage energy becomes

$$\delta E_B^* = E_B\delta B = \Phi_B. \tag{12}$$

Thus, the breakage dissipation Φ_B is linked to the area change of the grain size distribution from moving the current distribution function to a new position (Fig. 2b). Equation 12 indicates that energy dissipation from breakage is equivalent to the loss in residual breakage energy. Equation 9 was derived on the basis of the postulated breakage yielding criterion y and by considering Eq. 11

$$y = E_B^*(1-B) - E_c = E_B(1-B)^2 - E_c \leq 0. \tag{13}$$

The stresses p and q and breakage energy E_B become (with the aid of Eq. 1):

$$p = \frac{\partial \Psi}{\partial \varepsilon_v^e} = (1 - \vartheta B) K \varepsilon_v^e, \tag{14}$$

$$q = \frac{\partial \Psi}{\partial \varepsilon_s^e} = 3(1 - \vartheta B) G \varepsilon_s^e, \tag{15}$$

$$E_B = -\frac{\partial \Psi}{\partial B} = \frac{\vartheta}{2}\left(K\varepsilon_s^{e2} + 3G\varepsilon_s^{e2}\right). \tag{16}$$

In a similar way, the dissipative stresses $\left(\bar{p}, \bar{q}\right)$ and dissipative breakage energy $\bar{E}_B$ are obtained from the dissipation potential (Eq. 2):

$$\bar{p} = \frac{\partial \Phi}{\partial \delta \varepsilon_v^e} = \frac{\partial \Phi}{\partial \Phi_p^v}\frac{\partial \Phi_p^v}{\partial \delta \varepsilon_v^e} = \frac{\Phi_p^v}{\sqrt{\Phi_B^2 + \Phi_p^{v2} + \Phi_p^{s2}}}\frac{\partial \Phi_p^v}{\partial \delta \varepsilon_v^e}, \tag{17}$$

$$\bar{q} = \frac{\partial \Phi}{\partial \delta \varepsilon_s^e} = \frac{\partial \Phi}{\partial \Phi_p^s}\frac{\partial \Phi_p^s}{\partial \delta \varepsilon_s^e} = \frac{\Phi_p^s}{\sqrt{\Phi_B^2 + \Phi_p^{v2} + \Phi_p^{s2}}}\frac{\partial \Phi_p^s}{\partial \delta \varepsilon_s^e}, \tag{18}$$

$$\bar{E}_B = \frac{\partial \Phi}{\partial \delta B} = \frac{\partial \Phi}{\partial \Phi_B}\frac{\partial \Phi_B}{\partial \delta \varepsilon_B} = \frac{\Phi_B}{\sqrt{\Phi_B^2 + \Phi_p^{v2} + \Phi_p^{s2}}}\frac{\partial \Phi_B}{\partial \delta \varepsilon_B}. \tag{19}$$

The yield function y^* in generalized stress space is formulated in the following form

$$y^* = \left(\frac{\bar{E}_B}{\frac{\partial \Phi_B}{\partial \delta B}}\right)^2 + \left(\frac{\bar{p}}{\frac{\partial \Phi_p^v}{\partial \delta \varepsilon_v^p}}\right)^2 + \left(\frac{\bar{q}}{\frac{\partial \Phi_p^s}{\partial \delta \varepsilon_s^p}}\right)^2 - 1 \leq 0. \tag{20}$$

The following flow rules are obtained from Eq. 20 with the help of Eqs. (5–7) ($\delta\lambda$ is a non-negative multiplier):

$$\partial B = \delta\lambda \frac{\partial y}{\partial \bar{E}_B} = 2\delta\lambda \frac{\bar{E}_B (1-B)^2 \cos^2 \omega}{E_B E_c}, \tag{21}$$

$$\partial\varepsilon_v^p = \delta\lambda\frac{\partial y}{\partial \bar{p}} = 2\delta\lambda\frac{\bar{p}E_B(1-B)^2\sin^2\omega}{p^2E_c}, \tag{22}$$

$$\partial\varepsilon_s^p = \delta\lambda\frac{\partial y}{\partial \bar{q}} = 2\delta\lambda\frac{\bar{q}}{M^2p^2}. \tag{23}$$

Using the orthogonality condition $\left(p=\bar{p}, q=\bar{q}, E_B=\bar{E}_B\right)$, the flow rules become:

$$\partial B = 2\delta\lambda\frac{(1-B)^2\cos^2\omega}{E_c}, \tag{24}$$

$$\partial\varepsilon_v^p = 2\delta\lambda\frac{E_B(1-B)^2\sin^2\omega}{pE_c}, \tag{25}$$

$$\partial\varepsilon_s^p = 2\delta\lambda\frac{q}{M^2p^2}. \tag{26}$$

The breakage/yield function denoted as y in mixed stress-energy space can be rewritten (with the aid of Eqs. (20–23)) as

$$y = \frac{E_B\,(1-B)^2}{E_c} + \left(\frac{q}{Mp}\right)^2 - 1 \le 0. \tag{27}$$

Using Eqs. 14 and 15, the breakage energy in Eq. 16 is

$$E_B = \frac{\vartheta}{2\,(1-\vartheta B)^2}\left(\frac{p^2}{K}+\frac{q^2}{3G}\right). \tag{28}$$

Thus, the breakage/yield function has the following form on the basis of Eq. 28

$$y = \frac{\vartheta}{2E_c}\left(\frac{p^2}{K}+\frac{q^2}{3G}\right)\left(\frac{1-B}{1-\vartheta B}\right)^2 + \left(\frac{q}{Mp}\right)^2 - 1 \le 0. \tag{29}$$

The elastic moduli $K$and G are assumed to be inversely proportional to porosity n ($n = e/(1+e), e$ – void ratio)

$$K = \frac{K^*}{n} \text{ and } G = \frac{G^*}{n}. \tag{30}$$

During a breakage process ($y = 0$), the breakage variable B can be expressed as

$$B = \frac{1-f(p,q,n)}{1-\vartheta f(p,q,n)}, \tag{31}$$

where the breakage/yield function $f(p,q,n)$ is equal to

$$f(p,q,n) = \sqrt{\frac{2E_c}{n\vartheta} \times \frac{3G^*K^*\left[1-\left(\frac{q}{Mp}\right)^2\right]}{3G^*p^2+K^*q^2}} = p_c \sqrt{\frac{1}{n} \times \frac{\left[1-\left(\frac{q}{Mp}\right)^2\right]}{p^2+\frac{2(1+\nu)}{9(1-2\nu)}q^2}}, \quad (32)$$

with ν as the Poisson's ratio and p_c described by Eq. 10.

The average particle size can be approximately defined as d_{50} with the help of Eq. 4

$$d_{50} = (1-B)d_{50}^0 + Bd_{50}^u, \quad (33)$$

where d_{50}^u is the ultimate mean grain diameter calculated under the assumption that the grain size distribution tends to be fractal (Hardin 1985, McDowell and Bolton 1998) and d_{50}^0 denotes the initial mean grain diameter. Inserting Eq. 31 into Eq. 33, the change of the mean grain diameter d_{50} during deformation is calculated as

$$d_{50} = d_{50}^0 \frac{f}{1-\vartheta f} + d_{50}^u \frac{1-f}{1-\vartheta f} = d_{50}^u \frac{1+f\left[((1-\vartheta)R_d-1)\right]}{1-\vartheta f} \quad (34)$$

with the breakage/yield function f by Eq. 32 and

$$R_d = \frac{d_{50}^0}{d_{50}^u}, \quad (35)$$

$$d_{50}^u = \frac{3-\gamma}{4-\gamma} d_M, \quad (36)$$

$$d_{50}^0 = \frac{2}{3}\frac{d_M^3 - d_m^3}{d_M^2 - d_m^2}, \quad (37)$$

where d_m denotes the minimum initial grain diameter, d_M is the maximum initial grain diameter, γ stands for the fractal coefficient (taken usually between 2.5–2.8), and R_d represents the absolute mean grain size reduction from the initial to ultimate gsd. Equation 36 is calculated as the first order moment of the fractal grain size distribution $p_u(d)$

$$p_u(d) = \frac{(3-\gamma)}{d_M}\left(\frac{d}{d_M}\right)^{2-\gamma}. \quad (38)$$

obtained by differentiating the ultimate grain size cumulative function proposed by Turcotte (1986)

$$F_u(d) = \left(\frac{d}{d_M}\right)^{3-\gamma}. \tag{39}$$

In turn, Eq. 37 is calculated as the first order moment of the initial grain size distribution $p_0(d)$ (one assumes that the initial *gsd* is uniform in mass)

$$p_0(d) = 2\frac{d}{d_M^2 - d_m^2}. \tag{40}$$

Equations 32–37 are based directly on results from breakage mechanics. This theory, however, implies the existence of a yield surface, within which grain size reduction is not expected. Also, the process of breakage implies yielding. On the other hand, hypoplasticity avoids the notion of yield. Therefore, the function f (Eq. 32) requires adjustment, which will enable to consider continuous fabric changes. Here, a simple solution is given by introducing the function $f_d \equiv f_d(e)$ (Eq. 56), which, through the relative void ratio, weighs the material proximity to its critical (residual) state

$$f = c\sqrt{\left(\frac{1+e}{e}\right)\left(\frac{1-\left(\frac{f_d q}{Mp}\right)^2}{p^2 + \frac{2(1+\nu)}{9(1-2\nu)}q^2}\right)} \text{ with } f_d \equiv f_d(e) = \left(\frac{e-e_d}{e_c-e_d}\right)^{\alpha}. \tag{41}$$

The critical (residual) state implies that $e = e_c$, $q = Mp$, $f_d = 1$, and therefore $f = 0$, at which stage the grain size attains its ultimate state finest value d_{50}^u. These properties of the modified Eq. 41 provide quite a robust procedure to be included in hypoplasticity, which retains some of the theoretical advantages of breakage mechanics. The only remaining element to satisfy is that the grain size will constantly continue to decrease. This is guaranteed simply by continuously tracking the grain size measured using Eq. 34, while avoiding modifications to the grain size if the equation implies increasing grain sizes.

The calculations were performed with the minimum initial grain diameter d_m = 0.08 mm and the maximum initial grain diameter d_M = 0.80 mm. Thus, the initial mean grain diameter of sand was d_{50}^0 = 0.5 mm (Eq. 37) (as for Karlsruhe sand) and the ultimate mean grain diameter after breakage was d_{50}^u = 0.23 mm (Eq. 36). Other model parameters were assumed according to Einav and Valdes (2008): α = 2.6, ϑ = 0.85 and p_c = 1900 kPa. The Poisson's ratio was assumed to be ν = 0.3.

4. FE Input Data

The quasi-static plane strain FE-calculations were performed for an infinitely long and narrow granular strip of the height of h_0 = 10 mm ($h_0 = 20 \times d_{50}^0$) between

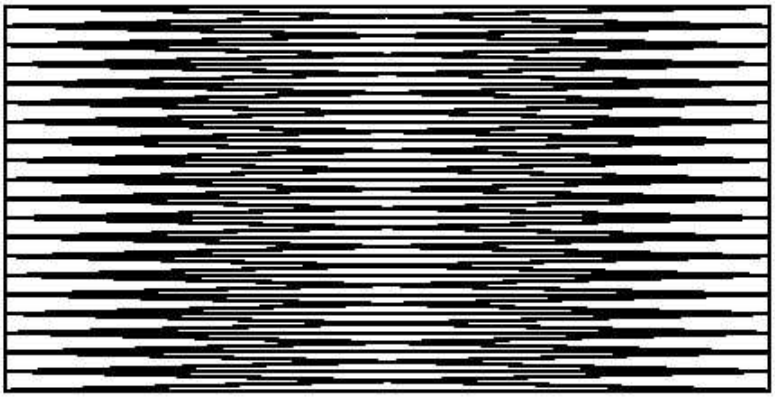

Fig. 3. FE mesh used for calculations: height 10 mm, width 100 mm (different scale is used in vertical and horizontal direction)

two rigid very rough walls under constant vertical pressure and conditions of free dilatancy. The study was performed with only one element column with a width of $b = 100$ mm, consisting of 20 quadrilateral horizontal elements, each composed of four diagonally crossed triangles (Fig. 3). In total, 80 triangular elements were used. The height of the finite elements $h_e = d_{50}^0 = 2 \times d_{50}^u$ was always smaller than $h_e \leq 5 \times d_{50}^0$ and $h_e \leq 5 \times d_{50}^u$ to obtain mesh-independent results (Tejchman 1989, Tejchman and Bauer 1996). To check the mesh-insensitivity, one comparative FE calculation was also carried out with one element column consisting of 40 quadrilateral horizontal elements, each composed of four diagonally crossed triangles (with $h_e = 0.5 \times d_{50}^0$). The behaviour of an infinite shear layer was modelled by lateral periodic boundary conditions, i.e. displacements and rotations along both sides of the column were the same (i.e. constrained by the same amount). Consequently, the evolution of the state variables was independent of the layer length. The integration was performed with three sampling points placed in the middle of each element side. Linear shape functions were used for displacements and for the Cosserat rotation (Tejchman 1989). The calculations were carried out with large deformations and curvatures using the so-called "updated Lagrangian" formulation by taking into account the Jaumann stress rate and Jaumann couple stress rate and the actual geometry and area of finite elements.

In hypoplasticity, an initial stress state is needed, since the stress rates depend on the stresses (Eqs. 45 and 46). The following insignificant initial stress state was assumed in the granular layer: $\sigma_{22}^0 = 1.0$ kPa and $\sigma_{11}^0 = \sigma_{33}^0 = 0.45$ kPa $\sigma_{11}^0/\sigma_{22}^0 = K_0 = 0.45$. Gravity was neglected. The initial void ratio of dense sand e_0 ($e_0 = 0.60$) or loose sand ($e_0 = 1.0$) was assumed to be homogeneous in the entire specimen. The dense sand specimen was subject to shearing with free dilatancy under constant vertical pressure of $p_v = 500$ kPa, $p_v = 2000$ kPa or $p_v = 5000$ kPa,

respectively. Shear deformation was initiated through constant horizontal displacement increments (directed to the left), prescribed only at the nodes along the top of the strip. The displacement increments were chosen as $\Delta u/h = 0.000025$. Thus, the three successive calculation phases could be distinguished: first, the initial stress state was prescribed in the granular specimen, second, constant vertical pressure was prescribed to the layer, and third, the layer was subjected to monotonic shearing.

The walls were assumed to be very rough (neither sliding nor rotation). The boundary conditions along the bottom were: $u_1 = 0$, $u_2 = 0$ and $\omega^c = 0$, and along the top boundary: $u_1 = n\Delta u$, $\omega^c = 0$, and $\sigma_{22} = p_v$ (the parameter n denotes the number of time steps and Δu is the constant displacement increment in one step).The lack of both rotation and slip along very rough walls was confirmed in several wall friction experiments (Uesugi 1987, Tejchman 1989, Löffelmann 1989, Tejchman and Wu 1995).

For the solution of the non-linear equation system, a modified Newton-Raphson scheme with line search is used. The global stiffness matrix was calculated with the first two terms of the constitutive equations, which are linear in d^c_{kl} and kd_{50} in Eqs. 50 and 51. To accelerate the calculations, the initial increments of displacement and Cosserat rotation during shearing were assumed to be equal to the converged incremental nodal displacement and rotation from the previous step. Due to the presence of the non-linear terms in the constitutive equation, this procedure turned out to be more efficient than the full Newton-Raphson method, where convergence problems occurred in the softening regime. The iteration steps were performed using translational and rotational convergence criteria. For time integration of stresses and couple stresses in single finite elements within micro-polar hypoplasticity, a simple one-step Euler forward scheme was applied (Tejchman 1989). The effect of the integration scheme on results was found to be insignificant.

5. FE Results

Figure 4 shows the evolution of the stress components σ_{ij} in the middle of the granular strip of initially dense sand ($e_0 = 0.60$) with the normalized horizontal displacement at the top u^t_1/h_0 ($h_0 = 10$ mm – layer height) and with grain crushing ($p_v = 2000$ kPa). In turn, Figure 5 presents the effect of grain crushing on the evolution of the mobilized wall friction angle ($\phi = \arctan \sigma_{12}/\sigma_{22}$) versus the shear deformation u^t_1/h_0 ($p_v = 2000$ kPa). The distribution of the Cosserat rotation ω^c (the positive Cosserat rotation (+ ω^c) is directed counterclockwise, Fig. 1) and void ratio e along the layer height at the residual state are demonstrated in Fig. 6. In addition, the distribution of normal stresses after prescribing vertical pressure (but before shearing), and distribution of stresses σ_{ij} and vertical couple stress m_2 along the layer height after monotonic shearing at the residual state is shown in Fig. 7. The evolution of the mean grain diameter across the granular strip during shearing and its distribution across the layer at the residual state is shown in Fig. 8. Finally,

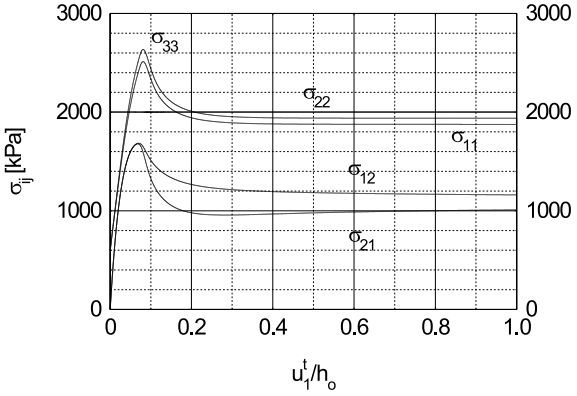

Fig. 4. Shearing of initially dense sand ($e_0 = 0.60$, $p_v = 2000$ kPa) between two very rough boundaries: evolution of stresses at the mid-point versus shear deformation u_1^t/h_0

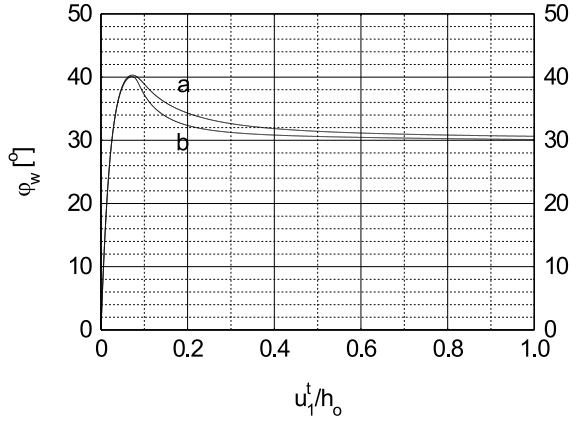

Fig. 5. Shearing of initially dense sand ($e_0 = 0.60$, $p_v = 2000$ kPa) between two very rough boundaries: evolution of wall friction angle ($\varphi_w = \arctan \sigma_{12}/\sigma_{22}$) versus shear deformation u_1^t/h_0: a) without grain crushing, b) with grain crushing (Eqs. 29–32)

the effect of the mesh size on the distribution of the Cosserat rotation is shown (Fig. 9).

Before shearing, the normal stress ratio is about $\sigma_{11}/\sigma_{22} = 0.6$ with $\sigma_{22} = p_v = 2000$ kPa (Fig. 6a). The material is subjected to densification due to compressive pressure p_v (from $e_0 = 0.60$ down to $e_0 = 0.52$). During monotonic shearing (as can be seen from Fig. 4), the normal stress σ_{22} always remains constant ($\sigma_{22} = p_v = 2000$ kPa). The remaining normal stresses σ_{11} and σ_{33} are initially smaller than σ_{22}, increase sharply to about 2500–2600 kPa at the displacement of about $u_1^t/h_0 \approx 0.2$ and decrease gradually with increasing displacement to approach the normal stress σ_{22}. The stress tensor becomes non-symmetric ($\sigma_{12} \neq \sigma_{21}$) after the peak. All normal stress ratios are equal to almost 1 at the residual state. The stresses

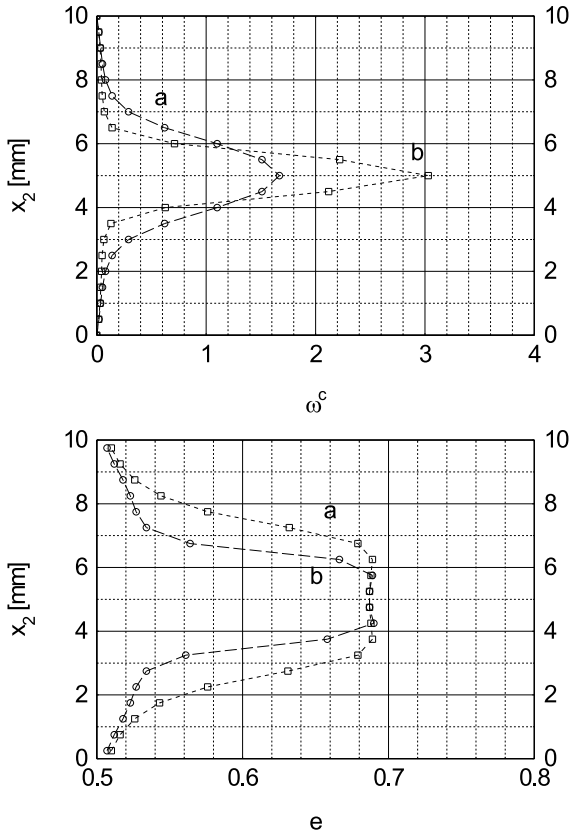

Fig. 6. Shearing of initially dense sand ($e_0 = 0.60$, $p_v = 2000$ kPa) between two very rough boundaries: distribution of Cosserat rotation ω^c and void ratio e across the layer height x_2 at residual state at $u_1^t/h_0 = 1$: a) without grain crushing, b) with grain crushing (Eqs. 29–32)

and wall friction angle tend to their asymptotic values (Figs. 4 and 5). The mobilized wall friction angle is $\phi_w = 40°$ at peak and $\phi_w = 30.5°$ at the residual state in the case of FE studies without grain crushing and $\phi_w = 40°$ (at peak) and $\phi_w = 30°$ (at the residual state) with grain crushing (Fig. 5). The obtained friction angles at peak and at the residual state are qualitatively in a satisfactory agreement with laboratory results with Karlsruhe sand carried out by Vardoulakis (1980) in plane strain compression. However, the calculated stiffness is higher before the peak than observed in experiments.

A shear zone is formed in the middle of the layer, which is characterized by the appearance of Cosserat rotation (Fig. 6a) and a strong increase of void ratio (Fig. 6b). At the upper and lower boundaries of the dilatant shear zone, a strong jump of the horizontal displacement, curvature, stresses and couple stress can be observed. The thickness of the shear zone (as visible from the Cosserat rotation) is about $t_s = 10 \times d_{50}^0$ (5 mm) without grain crushing and $t_s = 6 \times d_{50}^0$ (3 mm) with

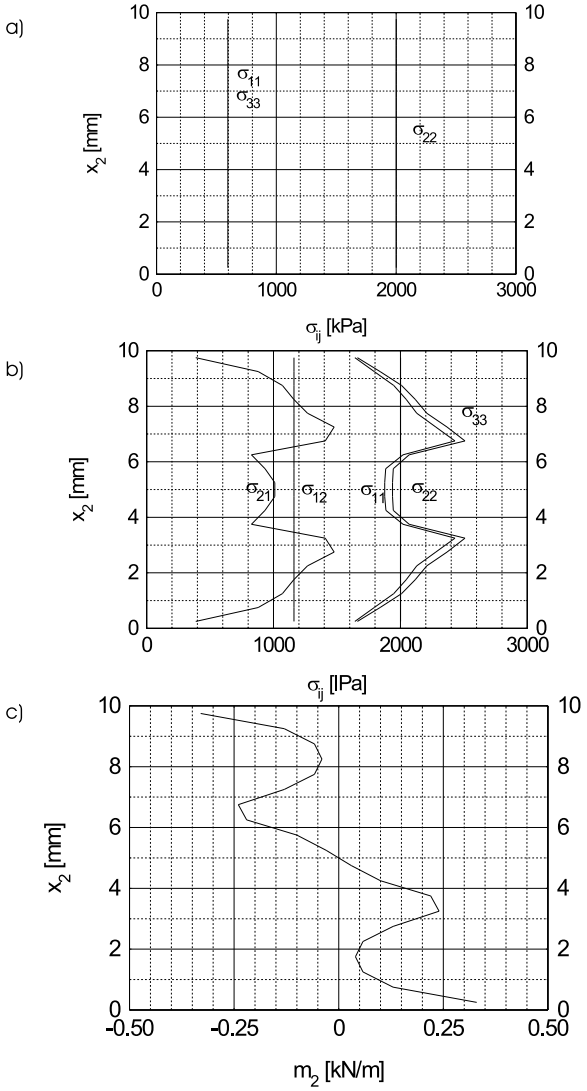

Fig. 7. Shearing of initially dense sand (e_0 = 0.60, p_v = 2000 kPa) between two very rough boundaries with grain crushing (Eqs. 34 and 41): a) distribution of stresses σ_{ij} across the layer height x_2 before shearing, b) distribution of stresses σ_{ij} and c) distribution of couple stress m_2 across the layer height x_2 after shearing at residual state at u_1^t/h_0 = 1

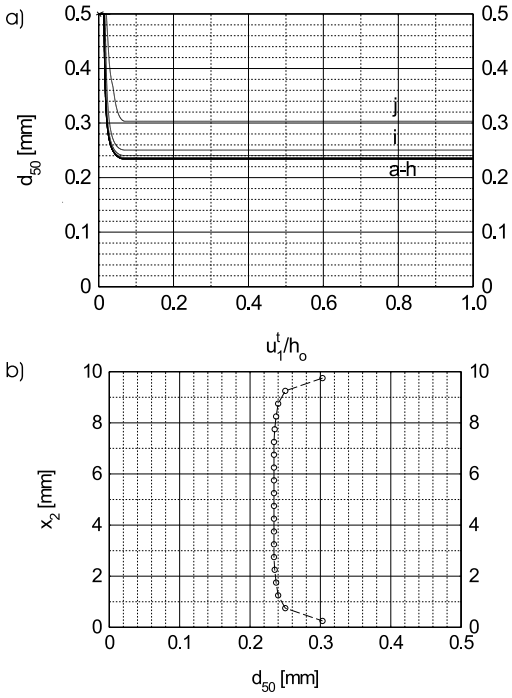

Fig. 8. Shearing of initially dense sand ($e_0 = 0.60$, $p_v = 2000$ kPa) between two very rough boundaries: A) evolution of grain diameter d_{50} versus shear deformation u_1^t/h_0 at: a) $x_2 = 4.75$ mm (mid-point), b) $x_2 = 4.25$ mm, c) $x_2 = 3.75$ mm, d) $x_2 = 3.25$ mm, e) $x_2 = 2.75$ mm, f) $x_2 = 2.25$ mm, g) $x_2 = 1.75$ mm, h) $x_2 = 1.25$ mm, i) $x_2 = 0.75$ mm, j) $x_2 = 0.25$ mm (wall), B) distribution of grain diameter d_{50} across the layer height x_2 at residual state at $u_1^t/h_0 = 1$

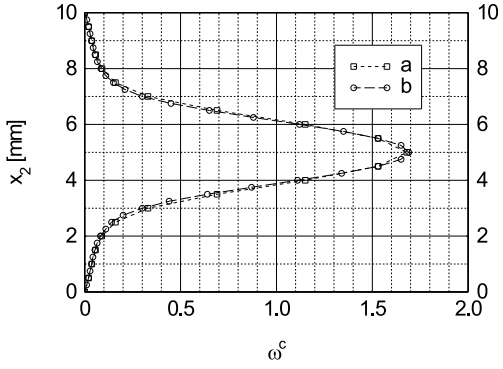

Fig. 9. Shearing of initially dense sand ($e_0 = 0.60$, $p_v = 2000$ kPa) between two very rough boundaries (without grain crushing): distribution of Cosserat rotation ω^c across the layer height x_2 at residual state at $u_1^t/h_0 = 1$: a) mesh with 80 quadrilateral elements of 0.5 mm height, b) mesh with 160 quadrilateral elements of 0.25 mm height

grain crushing. The void ratio increases in the middle of each shear zone at residual state up to $e_c = 0.69$. Outside the dilatant shear zone, the void ratio is about 0.54.

The distribution of stresses σ_{11}, σ_{33} and σ_{21} and the horizontal displacement u_1 across the shear zone is strongly non-linear (Fig. 7). The stresses σ_{11}, σ_{33} and σ_{21} in the shear zone show parabolic distribution. The stresses σ_{11} and σ_{33} have their minima and the stress σ_{21} their maxima in the middle of the shear zone. The distribution of m_2 is linear in the shear zone.

The reduction of the mean grain diameter d_{50} across the layer height is non-uniform (Fig. 8B) and takes place only in a hardening regime (Fig. 8A). The grains are continuously crushed towards the ultimate grain size in the entire shear zone during early stage of the shearing process. They decrease during shearing up to $u_1^t/h_0 = 0.07$ from $d_{50}^0 = 0.5$ mm down to $d_{50}^u = 0.23$ mm (in the shear zone) and from $d_{50}^0 = 0.5$ mm down to $d_{50} = 0.30$ mm outside the shear zone close to the horizontal boundaries. A similar outcome concerning a non-uniform reduction of d_{50} along the layer height with the maximum value in the mid-point of the shear zone and a significantly smaller one outside the shear zone was also obtained in laboratory experiments by Coop et al (2004).

The results of the distribution of Cosserat rotation (Fig. 9) show that the results with 80 and 160 finite elements are similar (thus, the effect of the mesh-size on the shear zone thickness is insignificant).

The effect of vertical pressure on the evolution of the wall friction angle and mean grain diameter is demonstrated in initially dense sand ($e_0 = 0.60$) with $p_v = 500$ kPa and $p_v = 5000$ kPa in Fig. 10. The results show that both the mean grain diameter and peak friction angle decrease with increasing p_v. The mean grain diameter decreases during shearing up to $u_1^t/h_0 = 0.07$ from $d_{50}^0 = 0.5$ mm down to $d_{50} \approx d_{50}^u = 0.26$ mm in the shear zone, and equals to $d_{50} = 0.43 - 0.50$ mm outside the shear zone close to the walls ($p_v = 500$ kPa). At large vertical pressure ($p_v = 5000$ kPa), the ultimate mean grain diameter $d_{50}^u = 0.23$ mm is reached across the entire granular strip. The thickness of the shear zone with crushable grains increases with increasing pressure and is (as visible from the Cosserat rotation) about $t_s = 4 \times d_{50}^0$ (2 mm) at $p_v = 500$ kPa and $t_s = 10 \times d_{50}^0$ (5 mm) at $p_v = 5000$ kPa (Fig. 11).

The effect of initial void ratio is demonstrated in Figs. 12–15 ($e_0 = 1.0$, $p_v = 500$ kPa). The material indicates insignificant softening (Fig. 12). At the beginning, initially loose sand is immediately subjected to strong densification due to high compressive pressure p_v (from $e_0 = 1.0$ down to $e_0 = 0.72$). The friction angle at peak decreases with increasing e_0 $\phi_w = 30.5^\circ$ at peak with $e_0 = 1.0$, Fig. 14. The residual friction angle is $\phi_w = 30^\circ$ (independently of initial void ratio). The thickness of the shear zone grows with increasing e_0 (from $t_s = 4 \times d_{50} = 2.0$ mm with $e_0 = 0.6$ up to $t_s = 12 \times d_{50} = 6.0$ mm with $e_0 = 1.0$), Fig. 15. The mean grain diameter decreases during shearing up to $u_1^t/h_0 = 0.07$ from $d_{50}^0 = 0.50$ mm down

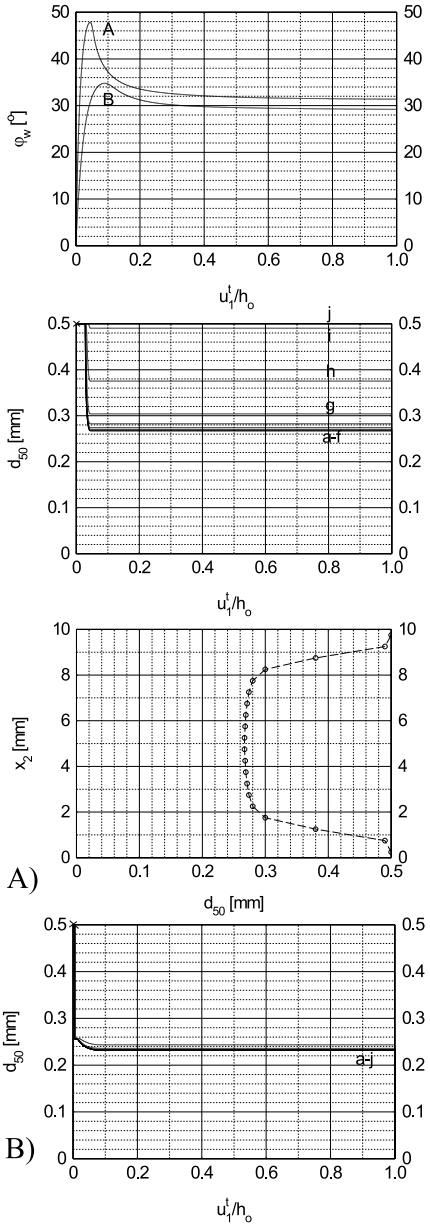

Fig. 10. Shearing of initially dense sand ($e_0 = 0.60$) between two very rough boundaries: evolution of wall friction angle φ_w and grain diameter d_{50} versus shear deformation u_1^t/h_0 at: a) $x_2 = 4.75$ mm (mid-point), b) $x_2 = 4.25$ mm, c) $x_2 = 3.75$ mm, d) $x_2 = 3.25$ mm, e) $x_2 = 2.75$ mm, f) $x_2 = 2.25$ mm, g) $x_2 = 1.75$ mm, h) $x_2 = 1.25$ mm, i) $x_2 = 0.75$ mm, j) $x_2 = 0.25$ mm (wall) and distribution of grain diameter d_{50} across the layer height x_2 at residual state at $u_1^t/h_0 = 1$ A) $p_v = 500$ kPa, B) $p_v = 5000$ kPa

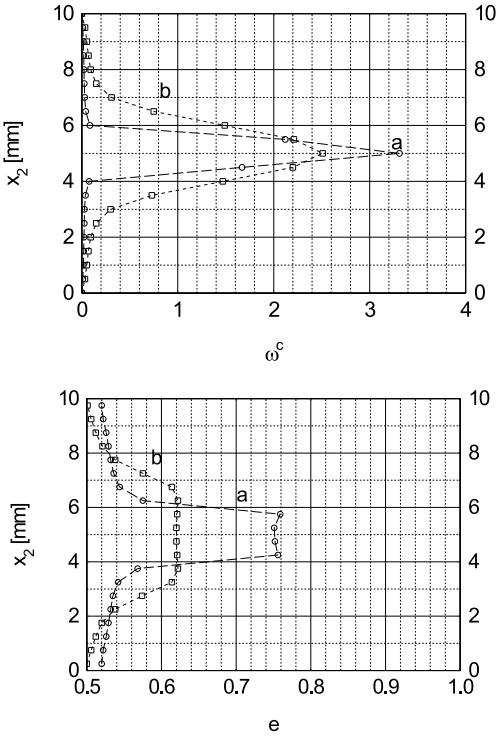

Fig. 11. Shearing of initially dense sand ($e_0 = 0.60$) between two very rough boundaries: distribution of Cosserat rotation ω^c and void ratio e across the layer height x_2 at residual state at $u_1^I/h_0 = 1$: a) $p_v = 500$ kPa, b) $p_v = 5000$ kPa

to $d_{50} = 0.32$ mm ($d_{50} > d_{50}^u$) in the shear zone. It does not vary outside the shear zone at the wall (Fig. 14). Thus, the reduction of the grain diameter is lower in initially loose sand. The stress tensor is slightly non-symmetric in initially loose sand (Fig. 13). The distribution of stresses across the layer is also slightly non-linear there (Fig. 13).

Table 1 summarizes the results of the shear zone thickness from FE calculations (as the function of e_0 and p_v).

Table 1. The results of the thickness of the shear zone from FE calculations (d_{50}^0 – initial mean grain diameter)

Initial void ratio e_0	Vertical pressure $p_v = 500$ kPa	Vertical pressure $p_v = 2000$ kPa	Vertical pressure $p_v = 5000$ kPa
0.60	2 mm $\left(4 \times d_{50}^0\right)$	3 mm $\left(6 \times d_{50}^0\right)$	5 mm $\left(10 \times d_{50}^0\right)$
1.00	6 mm $\left(12 \times d_{50}^0\right)$		

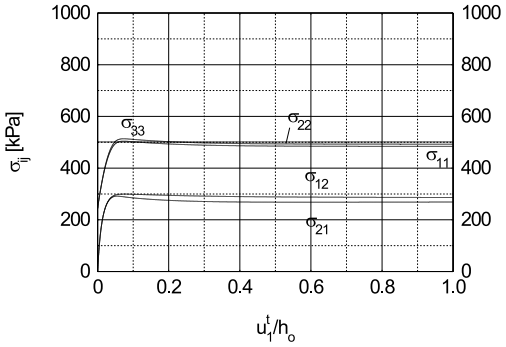

Fig. 12. Shearing of initially loose sand ($e_0 = 1.0$, $p_v = 500$ kPa) between two very rough boundaries: evolution of stresses at the mid-point versus shear deformation u_1^t/h_0

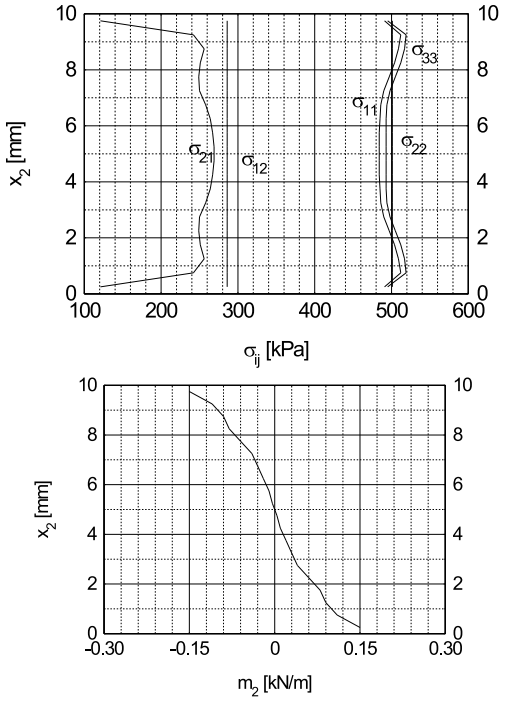

Fig. 13. Shearing of initially loose sand ($e_0 = 1.0$, $p_v = 500$ kPa) between two very rough boundaries with grain crushing: distribution of stresses σ_{ij} and couple stress m_2 across the layer height x_2 at residual state at $u_1^t/h_0 = 1$

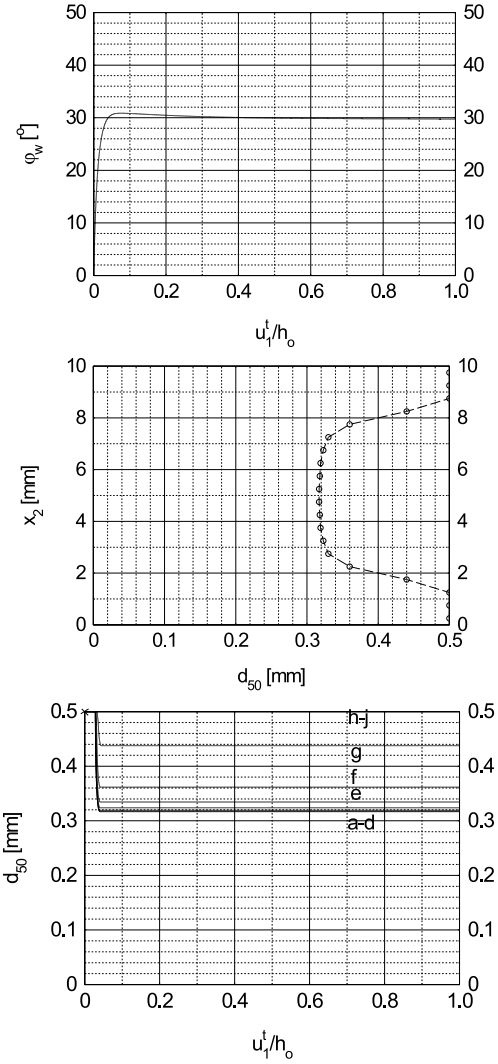

Fig. 14. Shearing of initially loose sand (e_0 = 1.0, p_v = 500 kPa) between two very rough boundaries: evolution of wall friction angle φ_w and grain diameter d_{50} versus shear deformation u_1^t/h_0 at: a) x_2 = 4.75 mm (mid-point), b) x_2 = 4.25 mm, c) x_2 = 3.75 mm, d) x_2 = 3.25 mm, e) x_2 = 2.75 mm, f) x_2 = 2.25 mm, g) x_2 = 1.75 mm, h) x_2 = 1.25 mm, i) x_2 = 0.75 mm, j) x_2 = 0.25 mm (wall) and distribution of grain diameter d_{50} across the layer height x_2 at residual state at u_1^t/h_0 = 1

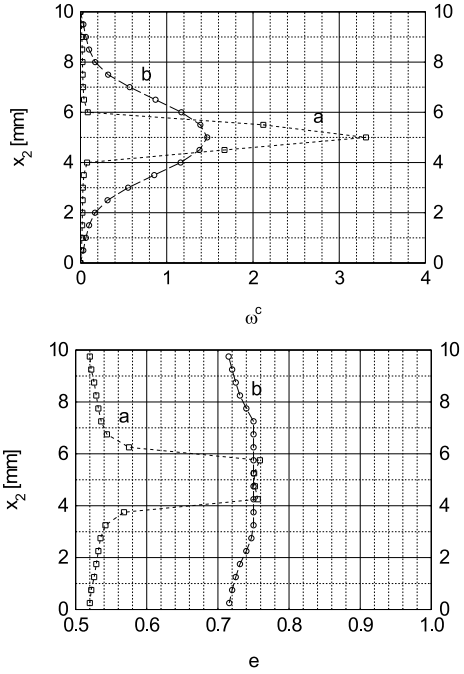

Fig. 15. Shearing of initially loose sand (p_v = 500 kPa) between two very rough boundaries: distribution of Cosserat rotation ω^c and void ratio e across the layer height x_2 at residual state at $u_1^t/h_0 = 1$: a) $e_0 = 0.60$, b) $e_0 = 1.0$

6. Conclusions

In the paper, the effect of grain crushing on the sand behaviour in the narrow granular strip during shearing under constant vertical pressure was numerically investigated. The results were qualitatively in agreement with experiments.

The numerical results show that the degree of particle breakage affects the sand behaviour after the peak only. The thickness of the shear zone significantly decreases with grain crushing. In turn, the mobilized residual shear resistance decreases insignificantly. The mean grain diameter decreases more strongly in the shear zone than outside it, and more strongly in initially loose sand than in initially dense sand. The thickness of the shear zone inside of a granular strip increases with increasing initial void ratio. In initially dense sand, it increases with increasing pressure.

The next research will be focused on taking into account grain crushing within micro-polar hypoplasticity only (by modification of a grain diameter change similarly to a change of void ratios by Eqs. 57–59). The initial grain diameter will be stochastically distributed using a spatially correlated random field (Tejchman and Górski 2008).

Appendix

The constitutive relationship between the rate of stress, the rate of couple stress, the strain rate and the curvature rate can be generally expressed by the following two equations (Tejchman and Gudehus 2001, Tejchman 2004, Tejchman and Wu 2007):

$$\overset{\circ}{\sigma}_{ij} = F_{ij}(e, \sigma_{kl}, m_i, d^c_{kl}, k_i, d_{50}), \tag{42}$$

$$\overset{\circ}{m}_i = G_i(e, \sigma_{kl}, m_i, d^c_{kl}, k_i, d_{50}). \tag{43}$$

The Jaumann stress rate and Jaumann couple stress rate therein are defined by

$$\overset{\circ}{\sigma}_{ij} = \overset{\bullet}{\sigma}_{ij} - w_{ik}\sigma_{kj} + \sigma_{ik}w_{kj} \tag{44}$$

and

$$\overset{\circ}{m}_i = \overset{\bullet}{m}_i - 0.5w_{ik}m_k + 0.5m_k w_{ki}. \tag{45}$$

The functions F_{ij} and G_i in Eqs. 37 and 38 represent isotropic tensor-valued functions of their arguments; σ_{ij} is the Cauchy stress tensor, m_i is the couple stress vector, e denotes the current void ratio, d^c_{kl} is the polar strain rate and k_i denotes the rate of curvature vector:

$$d^c_{ij} = d_{ij} + w_{ij} - w^c_{ij}, \text{ and } k_i = w^c_{,i}. \tag{46}$$

The rate of deformation tensor d_{ij} and the spin tensor w_{ij} are related to the velocity v_i as follows:

$$d_{ij} = \frac{v_{i,j} + v_{j,i}}{2}, \quad w_{ij} = \frac{v_{i,j} - v_{j,i}}{2}, \quad ()_{,i} = \frac{\partial()}{\partial x_i}. \tag{47}$$

The rate of Cosserat rotation w^c is defined by

$$w^c_{21} = -w^c_{12} = w^c \text{ and } w^c_{kk} = 0. \tag{48}$$

For moderate pressures, the grains can be assumed to be isochoric. In this case, the change of void ratio depends only on the strain rate via

$$\overset{\bullet}{e} = (1 + e)d_{kk}. \tag{49}$$

For the numerical calculations, the following micro-polar hypoplastic constitutive equations are employed

$$\overset{\circ}{\sigma}_{ij} = f_s \left[{}_{ij}\left(\hat{\sigma}_{kl}, \hat{m}_k, d^c_{kl}, k_k d_{50}\right) + f_d N_{ij}\left(\hat{\sigma}_{ij}\right) \sqrt{d^c_{kl}d^c_{kl} + k_k k_k d^2_{50}} \right] \tag{50}$$

and

$$\frac{\overset{\circ}{m}_i}{d_{50}} = f_s \left[{}^{c}_{i}\left(\hat{\sigma}_{kl}, \hat{m}_k, d^c_{kl}, k_k d_{50}\right) + f_d N^c_i \left(\hat{m}_i\right) \sqrt{d^c_{kl} d^c_{kl} + k_k k_k d^2_{50}} \right], \tag{51}$$

wherein the normalized stress tensor $\hat{\sigma}_{ij}$ is defined by

$$\hat{\sigma}_{ij} = \frac{\sigma_{ij}}{\sigma_{kk}} \tag{52}$$

and the normalized couple stress vector $\hat{m}_i$ is defined by

$$\hat{m}_i = \frac{m_i}{\sigma_{kk} d_{50}}, \tag{53}$$

wherein d_{50} is the mean grain diameter. The scalar factors $f_s = f_s(e, \sigma_{kk})$ and $f_d = f_d(e, \sigma_{kk})$ in Eqs. 50 and 51 describe the influence of density and stress level on the incremental stiffness. The factor f_s depends on the granulate hardness h_s, the mean stress σ_{kk}, the maximum void ratio e_i and the current void ratio e by:

$$f_s = \frac{h_s}{n h_i} \left(\frac{1 + e_i}{e_i} \right) \left(\frac{e_i}{e} \right)^{\beta} \left(-\frac{\sigma_{kk}}{h_s} \right)^{1-n} \tag{54}$$

with

$$h_i = \frac{1}{c_1^2} + \frac{1}{3} - \left(\frac{e_{i0} - e_{d0}}{e_{c0} - e_{d0}} \right)^{\alpha} \frac{1}{c_1 \sqrt{3}}. \tag{55}$$

In the above equations, the granulate hardness h_s represents a reference pressure, the coefficients α and β express the dependence on density and pressure respectively, and n denotes the compression coefficient. The multiplier f_d represents the dependence on a relative void ratio via:

$$f_d = \left(\frac{e - e_d}{e_c - e_d} \right)^{\alpha}. \tag{56}$$

The relative void ratio in the above expression involves the void ratio in critical state e_c, the minimum void ratio e_d (the densest packing) and the maximum void ratio e_i (the loosest packing). In a critical state, a granular material experiences continuous deformation while the void ratio remains unchanged. The current void ratio e is bounded by the two extreme void ratios e_i and e_d. Based on experimental observations, the void ratios e_i, e_d and e_c are assumed to depend on the pressure σ_{kk} (Bauer 1996):

$$e_i = e_{i0} \exp\left[-\left(-\frac{\sigma_{kk}}{h_s} \right)^{n} \right], \tag{57}$$

$$e_d = e_{d0} \exp\left[-\left(-\frac{\sigma_{kk}}{h_s}\right)^n\right], \tag{58}$$

$$e_c = e_{c0} \exp\left[-\left(-\frac{\sigma_{kk}}{h_s}\right)^n\right], \tag{59}$$

wherein e_{i0}, e_{d0} and e_{c0} are the values of e_i, e_d and e_c at $\sigma_{kk} = 0$, respectively. For the functions L_{ij}, N_{ij}, L_i^c and N_i^c, the following specific expressions are used:

$$L_{ij} = a_1^2 d_{ij}^c + \hat{\sigma}_{ij}\left(\hat{\sigma}_{kl} d_{kl}^c + \hat{m}_k k_k d_{50}\right), \tag{60}$$

$$L_i^c = a_1^2 k_i d_{50} + a_1^2 \hat{m}_i\left(\hat{\sigma}_{kl} d_{kl}^c + \hat{m}_k k_k d_{50}\right), \tag{61}$$

$$N_{ij} = a_1\left(\hat{\sigma}_{ij} + \hat{\sigma}_{ij}^*\right), \tag{62}$$

$$N_i^c = a_1^2 a_c \hat{m}_i, \tag{63}$$

where

$$a_1^{-1} = c_1 + c_2\sqrt{\hat{\sigma}_{kl}^* \hat{\sigma}_{lk}^*}[1 + \cos(3\theta)], \tag{64}$$

$$\cos(3\theta) = -\frac{\sqrt{6}}{\left[\hat{\sigma}_{pq}^* \hat{\sigma}_{pq}^*\right]^{1.5}}\left(\hat{\sigma}_{kl}^* \hat{\sigma}_{lm}^* \hat{\sigma}_{mk}^*\right) \tag{65}$$

with

$$c_1 = \sqrt{\frac{3}{8}}\frac{(3 - \sin\phi_c)}{\sin\phi_c}, \quad c_2 = \frac{3}{8}\frac{(3 + \sin\phi_c)}{\sin\phi_c}. \tag{66}$$

The parameter a_1 is the deviatoric part of the normalized stress in critical states (Bauer 1996), ϕ_c is the friction angle in critical states, the parameter θ denotes the Lode angle in the deviatoric plane at $\hat{\sigma}_{ii} = 1$, and $\hat{\sigma}_{ij}^*$ denotes the deviatoric part of $\hat{\sigma}_{ij}$.

References

Arslan H., Baykal G., Sture S. (2009) Analysis of the influence of crushing on the behaviour of granular materials under shear, *Granular Matter*, **11**, 87–97.

Bauer E. (1996) Calibration of a comprehensive hypoplastic model for granular materials, *Soils and Foundations*, **36** (1), 13–26.

Cheng Y. P., Nakata Y., Bolton M. D. (2003) Discrete element simulation of crushable soil, *Geotechnique*, **53** (7), 633–641.

Coop M. R., Sorensen K. K., Boda Freitas T., Georgoutsos G. (2004) Particle breakage during shearing of a carbonate sand, *Geotechnique*, **54** (3), 157–163.

Einav I. (2007a) Breakage mechanics, Part I Theory, *J. Mech. Phys. Solids*, **55** (6), 1274–1297.

Einav I. (2007b) Breakage mechanics, Part II Modeling granular materials, *J. Mech. Phys. Solids*, **55** (6), 1298–1320.

Einav I. (2007c) Soil mechanics: breaking ground, *Proceedings of the Royal Society A: Mathematical, Physical and Engineering Sciences*, 365, 2985–3002.

Einav I., Valdes J. R. (2008) On comminution and yield in brittle granular mixtures, *J. Mech. Phys. Solids*, **55** (6), 2136–2148.

Gudehus G. (1996) A comprehensive constitutive equation for granular materials, *Soils and Foundations*, **36** (1), 1–12.

Hardin B. O. (1985) Crushing of soil particles, *J. Geotech. Eng. ASCE*, **111** (10), 1177–1192.

Herle I. and Gudehus G. (1999) Determination of parameters of a hypoplastic constitutive model from properties of grain assemblies, *Mechanics of Cohesive-Frictional Materials*, **4** (5), 461–486.

Indraratna B., Salim W. (2002) Modelling of particle breakage of coarse aggregates incorporating strength and dilatancy, *Geotechnical Engineering*, **155** (4), 243–252.

Löffelmann F. (1989) Theoretische und experimentelle Untersuchungen zur Schüttgut-Wand--Wechselwirkung und zum Mischen und Entmischen von Granulaten, *Publication Series of the Institut für Mechanische Verfahrenstechnik*, Universität Karlsruhe.

Marketos G., Bolton M. D. (2007) Quantifying the extent of crushing in granular materials: a probability-based predictive method, *J. Mech. Phys. Solids*, **55**, 2141–2156.

McDowell G. R., Bolton M. D., Robertson D. (1996) The fractal crushing of granular materials, *J. Mech. Phys. Solids*, **44** (12), 2079–2102.

McDowell G. R., Bolton M. D. (1998) On the micromechanics of crushable aggregates, *Geotechnique*, **48** (5), 667–679.

Miura N., O'Hara S. (1979) Particle crushing of a decomposed granite soil under shear stresses, *Soils and Foundation*, **19** (3), 1–14.

Nakata Y., Hyodo M., Hyde A. F. L., Kato Y., Murata K. (2001) Microscopic particle crushing of sand subjected to high pressure one-dimensional compression, *Soil and Foundations*, **41** (1), 69–82.

Oda M. (1993) Micro-fabric and couple stress in shear bands of granular materials, In: *Powders and Grains* (ed.: C. Thornton), Rotterdam, Balkema, 161–167.

Pasternak E., Mühlhaus H. B. (2001) Cosserat continuum modelling of granulate materials. In: *Computational Mechanics – New Frontiers for New Millennium* (eds.: S. Valliappan S. and N. Khalili), Elsevier Science, 1189–1194.

Schäfer H. (1962) Versuch einer Elastizitätstheorie des zweidimensionalen ebenen Cosserat--Kontinuums, *Miszellaneen der Angewandten Mechanik*, Festschrift Tolmien, W., Berlin, Akademie-Verlag.

Tejchman J. (1989) Scherzonenbildung und Verspannungseffekte in Granulaten unter Berücksichtigung von Korndrehungen, *Publication Series of the Institute of Soil and Rock Mechanics,* University Karlsruhe, 117, 1–236.

Tejchman J., Wu W. (1995) Experimental and numerical study of sand-steel interfaces, *Int. Journal of Numerical and Anal. Methods in Geomechanics*, **19** (8), 513–537.

Tejchman J., Bauer E. (1996) Numerical simulation of shear band formation with a polar hypoplastic model, *Computers and Geotechnics*, **19** (3), 221–244.

Tejchman J., Gudehus G. (2001) Shearing of a narrow granular strip with polar quantities, *Int. J. Num. and Anal. Methods in Geomechanics*, 25, 1–28.

Tejchman J. (2004) Influence of a characteristic length on shear zone formation in hypoplasticity with different enhancements, *Computers and Geotechnics*, **31** (8), 595–611.

Tejchman J., Wu W. (2007) Modeling of textural anisotropy in granular materials with stochastic micro-polar hypoplasticity, *Int. Journal of Non-linear Mechanics*, **42**, 882–894.

Tejchman J., Górski J. (2008) Computations of size effects in granular bodies within micro-polar hypoplasticity during plane strain compression, *Int. Journal for Solids and Structures*, **45** (6), 1546–1569.

Tejchman J., Wu W. (2009) FE-investigations of non-coaxiality and stress-dilatancy rule in dilatant granular bodies within micro-polar hypoplasticity, *Int. Journal for Numerical and Analytical Methods in Geomechanics*, **33** (1), 117–142.

Turcotte D. I. (1986) Fractals and Fragmentation, *J. Geophys. Res*., **91**, 1921–1926.

Uesugi M. (1987) Friction between dry sand and construction, *PhD Thesis,* Tokyo Institute of Technology.

Wu W., Niemunis A. (1996) Failure criterion, flow rule and dissipation function derived from hypoplasticity, *Mech. Cohes.-Frict. Mater.*, 1, 145–163.

Vallejo L. E., Lobo-Guerrero S. (2009) Fractal fragmentation of granular materials under compression *Powders and Grains*, AIP, 847–851.

Vardoulakis I. (1980) Shear band inclination and shear modulus in biaxial tests, *Int. J. Num. Anal. Meth. Geomech.*, 4, 103–119.

Yamamuro J. A., Lade P. V. (1998) Steady-state concepts and static liquefaction of silty sands, *J. Geotech. Geoenviron. Eng. ASCE*, **124**, 868–877.